Applied Science, Computing and Energy, 2026, 4(6), 1008-1030

Biogenic Synthesis and Characterization of MgO-Modified ZnO Nanocomposite for Photocatalytic Applications

Abdulazeez Monday Abdulrahman, Sumaila Abdulmumuni, Yahaya Muhammad Kabir and Sumaila Ahmed Onimisi

Received: 04 June 2026/Accepted: 20 August 2026/ Published: 24 August 2026

Abstract*: This study reports the biogenic synthesis and characterization of an MgO-modified ZnO nanocomposite as a sustainable material with potential application in photocatalytic wastewater treatment.* Moringa oleifera *leaf extract was employed as a biogenic reducing and stabilizing agent during the co-precipitation process, while NaOH facilitated hydroxide formation. MgO nanoparticles, ZnO nanoparticles, and MgO–ZnO nanocomposite were synthesized and subsequently calcined at 500 °C for 3 h. The synthesized materials were characterized using UV–Visible spectroscopy, high-resolution scanning electron microscopy (HRSEM), energy-dispersive X-ray spectroscopy (EDS), and X-ray diffraction (XRD). The UV–Visible absorption maxima occurred at 305, 302, and 298 nm for MgO, ZnO, and MgO–ZnO, respectively, corresponding to photon energies of 4.07, 4.11, and 4.16 eV. HRSEM revealed aggregated and rough morphologies for MgO and ZnO, whereas the MgO–ZnO nanocomposite exhibited a highly interconnected and textured nanoscale morphology with reduced apparent agglomeration and close interfacial contact between the constituent phases. EDS confirmed the presence of Mg, Zn, and O in the composite, with only a minor carbon signal. XRD analysis identified cubic MgO with reflections corresponding to JCPDS Card No. 45-0946 and hexagonal wurtzite ZnO corresponding to JCPDS Card No. 36-1451. The average crystallite sizes were 24.5 nm for MgO, 28.6 nm for ZnO, and 26.1 nm for the MgO–ZnO nanocomposite. The results demonstrate that incorporation of MgO produced measurable changes in the optical, morphological, elemental, and crystallographic characteristics of ZnO. The biogenic MgO–ZnO nanocomposite therefore provides a low-cost and environmentally compatible platform for further investigation in photocatalytic removal of organic pollutants from wastewater.*

Keywords: *MgO–ZnO; Biogenic synthesis;* Moringa oleifera*; Photocatalysis; Nanocomposite.*

Abdulazeez Monday Abdulrahman
Department of Chemistry, Confluence University of Science and Technology, Osara, Kogi State, Nigeria.
Email: abdulazeezma@custech.edu.ng

Sumaila Abdulmumuni
Department of Chemistry, Confluence University of Science and Technology, Osara, Kogi State, Nigeria.
Email: sumailaa@custech.edu.ng
https://orcid.org/0000-0001-5934-9440

Yahaya Muhammad Kabir
Department of Chemistry, Confluence University of Science and Technology, Osara, Kogi State, Nigeria.
Email: yahayakm@custech.edu.ng

Sumaila Ahmed Onimisi
Department of Chemistry, Confluence University of Science and Technology, Osara, Kogi State, Nigeria.
Email: sumailaao@custech.edu.ng

1.0 Introduction

The rapid expansion of industrial activities in sectors such as textile manufacturing, leather processing, food processing, pharmaceuticals, and other chemical-based industries has increased the discharge of synthetic dyes into aquatic environments. Common dyes, including methylene blue, rhodamine B, and bromophenol blue, are of environmental concern because of their complex aromatic structures, high chemical stability, and poor biodegradability, which enable them to persist in water and wastewater for extended periods (Sivaranjani et al., 2022). Their presence in

aquatic systems can reduce light penetration, interfere with photosynthetic processes, and produce toxic effects on aquatic organisms and humans (Ahmed et al., 2023). Consequently, the effective removal of dye contaminants from wastewater is essential for protecting water quality and reducing their potential ecological and human-health impacts.

Several conventional wastewater-treatment approaches, including adsorption, coagulation, membrane filtration, and biological treatment, have been employed for the removal of dyes. However, these methods may have limitations such as incomplete degradation, generation of secondary waste, high operational costs, or reduced effectiveness against chemically stable dye molecules, particularly at low concentrations. Photocatalytic degradation has therefore attracted considerable attention as an advanced oxidation process (AOP) for the treatment of persistent organic pollutants. In photocatalysis, semiconductor materials absorb photons with sufficient energy to generate electron–hole pairs. These charge carriers can participate in surface reactions that produce reactive oxygen species (ROS), particularly hydroxyl radicals (•OH) and superoxide radicals ($O_2^{\bullet -}$), which attack complex organic molecules and promote their transformation into less harmful products (Sarmah et al., 2021). The effectiveness of this process is strongly influenced by the structural, optical, surface, and electronic properties of the photocatalyst.

Among the semiconductor photocatalysts investigated for wastewater treatment, zinc oxide (ZnO) has received considerable attention because of its relatively low cost, abundance, chemical stability, and suitable photocatalytic properties. ZnO possesses a wide band gap of approximately 3.2 eV and can generate highly reactive charge carriers under appropriate irradiation conditions. Nevertheless, the practical application of ZnO photocatalysts is constrained by several factors, including limited absorption of visible light and rapid recombination of photogenerated electron–hole pairs, which can substantially reduce the number of charge carriers available for surface oxidation and reduction reactions (Deng et al., 2020). Consequently, considerable research has focused on modifying ZnO through doping, coupling, and heterostructure formation with other semiconducting materials to improve charge separation, surface properties, light utilization, and overall photocatalytic efficiency.

Magnesium oxide (MgO) is one of the metal oxides that has attracted interest for modification of ZnO because of its basic surface characteristics, chemical stability, and potential to alter the interfacial and surface properties of ZnO. Incorporation of MgO into ZnO can promote the development of interfacial structures that influence charge-carrier migration and separation, while modification of the surface may provide additional active sites for photocatalytic reactions (Kumar et al., 2022). The combination of the two oxides may therefore provide physicochemical characteristics that differ from those of the individual MgO and ZnO components. Such modifications are particularly relevant to photocatalytic applications because suppression of electron–hole recombination and improvement of surface reactivity can increase the availability of reactive species for the degradation of organic pollutants. However, the photocatalytic properties of MgO–ZnO materials depend strongly on their composition, crystallinity, particle size, morphology, and preparation conditions.

In addition to compositional modification, increasing attention has been directed toward environmentally benign methods for synthesizing metal-oxide nanomaterials. Conventional chemical synthesis may involve reducing, precipitating, capping, or stabilizing

agents that can be hazardous, expensive, or environmentally undesirable. Biogenic synthesis using plant extracts provides an alternative approach because naturally occurring phytochemicals, including phenolic compounds, flavonoids, proteins, carbohydrates, and other biomolecules, can participate in the reduction, complexation, stabilization, and capping of developing nanoparticles. Plant-mediated synthesis can consequently reduce the use of potentially hazardous synthetic reagents and may provide a relatively simple and cost-effective route for producing nanomaterials (Reddy et al., 2022; Verma et al., 2023). The use of readily available plant materials is also attractive for developing sustainable nanotechnology approaches, particularly in regions where low-cost and locally accessible resources are desirable.

Despite the growing body of research on ZnO photocatalysts, MgO-modified semiconductor materials, and plant-mediated nanoparticle synthesis, an important research gap remains concerning the integration of these approaches into the biogenic preparation of MgO-modified ZnO nanocomposites. In particular, comparatively limited information is available on the use of *Moringa oleifera* leaf extract as a biogenic medium for the synthesis of MgO–ZnO nanocomposites and on the resulting structural, optical, morphological, and elemental characteristics of the material. This gap is important because the phytochemical composition of a plant extract can influence nucleation, particle growth, surface stabilization, crystallinity, and particle aggregation, thereby affecting the properties and potential performance of the resulting photocatalyst. Establishing the characteristics of MgO-modified ZnO produced through a *Moringa oleifera*-mediated route can therefore provide useful information on the feasibility of combining semiconductor modification with a greener synthesis strategy.

Therefore, this study aimed to synthesize MgO-modified ZnO nanocomposites using *Moringa oleifera* leaf extract through a biogenic co-precipitation approach and to characterize the synthesized materials using UV-Visible spectroscopy, high-resolution scanning electron microscopy (HRSEM), energy-dispersive X-ray spectroscopy (EDS), and X-ray diffraction (XRD). The significance of the study lies in demonstrating a potentially simple, low-cost, and environmentally compatible route for producing MgO–ZnO nanocomposites with physicochemical characteristics relevant to photocatalytic applications. The study also contributes to the broader development of sustainable nanomaterial synthesis by utilizing a plant-based resource and reducing reliance on conventional chemical synthesis routes. The resulting MgO–ZnO material may provide a promising basis for the development of alternative photocatalysts for the treatment of dye-contaminated wastewater.

2.0 Materials and Methods

2.1 Materials

Analytical-grade zinc nitrate hexahydrate ($Zn(NO_3)_2 \cdot 6H_2O$), magnesium nitrate hexahydrate ($Mg(NO_3)_2 \cdot 6H_2O$), sodium hydroxide (NaOH), and sodium dodecyl sulfate (SDS) were used as received without further purification. *Moringa oleifera* leaves were obtained locally and thoroughly washed with distilled water to remove adhering dust and impurities. The leaves were subsequently air-dried, pulverized into a fine powder, and stored in a clean, dry container until required for the preparation of the plant extract.

2.2 Methods

2.2.1 Preparation of Moringa oleifera Leaf Extract

Approximately 25 g of the powdered *Moringa oleifera* leaves was added to 250 mL of distilled water and heated at boiling temperature for 20 min. The resulting mixture was allowed to cool to room temperature and

subsequently filtered through Whatman No. 1 filter paper to remove the plant residues. The filtrate was collected and stored appropriately for subsequent use as the biogenic reducing, capping, and stabilizing agent during the synthesis of the MgO-modified ZnO nanocomposite (Bognár et al., 2022).

2.2.2 Preparation of MgO Nanoparticles

MgO nanoparticles were prepared using a precipitation approach. Briefly, 1.8 g of magnesium nitrate hexahydrate was dissolved in 100 mL of deionized water to obtain the precursor solution. Subsequently, 10 mL of 0.1 M NaOH solution was added to the precursor under continuous stirring to promote the formation of a magnesium hydroxide precipitate. The resulting precipitate was separated, washed thoroughly with distilled water to remove residual ions, and subjected to drying and thermal treatment to obtain MgO nanoparticles. The conditions used for drying and calcination should be specified according to the actual experimental procedure.

2.2.3 Synthesis of ZnO Nanoparticles

ZnO nanoparticles were synthesized using a modified precipitation/sol–gel approach. Briefly, 100 mL of 0.02 M aqueous $Zn(NO_3)_2 \cdot 6H_2O$ solution was prepared, after which 5 mL of 0.02 M sodium dodecyl sulfate (SDS) solution was added as a surfactant and capping agent. Subsequently, 10 mL of 0.2 M NaOH solution was added dropwise under continuous stirring to promote the formation of the zinc-containing precipitate. The resulting precipitate was collected and thoroughly washed with distilled water to remove unreacted precursor ions and residual surfactant. The washed precipitate was subsequently vacuum-dried and thermally treated to obtain ZnO nanoparticles. The drying and calcination conditions should be reported according to the actual experimental procedure.

2.2.4 Biogenic Synthesis of MgO-Modified ZnO Nanocomposite

The MgO-modified ZnO nanocomposite was synthesized using a biogenic co-precipitation approach adapted from Morgan and Aboshanab (2024). Briefly, 100 mL of 0.1 M aqueous $Zn(NO_3)_2 \cdot 6H_2O$ solution was prepared, and $Mg(NO_3)_2 \cdot 6H_2O$ corresponding to 5 mol% Mg relative to the Zn precursor was added under continuous stirring. The exact mass or volume of the magnesium precursor used was calculated based on the desired Mg/Zn molar ratio.

Subsequently, 50 mL of the prepared *Moringa oleifera* leaf extract was added gradually to the precursor mixture under continuous stirring at 60 °C. Thereafter, 5 mL of 1 M NaOH solution was added to promote precipitation. The resulting suspension was maintained under stirring and subsequently allowed to age for 24 h. The precipitated material was then separated by filtration, thoroughly washed with distilled water, and dried at 100 °C for 6 h. The dried precursor was calcined at 500 °C for 3 h to facilitate the formation and crystallization of the MgO–ZnO nanocomposite. The resulting powder was allowed to cool to room temperature and stored in a clean, dry container prior to characterization.

2.3 Characterization of the Biogenically Synthesized Photocatalysts

The synthesized MgO nanoparticles, ZnO nanoparticles, and MgO-modified ZnO nanocomposite were characterized using high-resolution scanning electron microscopy coupled with energy-dispersive X-ray spectroscopy (HRSEM–EDS), X-ray diffraction (XRD), and ultraviolet–visible (UV–Vis) spectroscopy.

HRSEM was used to examine the surface morphology, particle shape, degree of agglomeration, and approximate particle-size distribution of the synthesized materials, while EDS was employed to determine their elemental composition. XRD analysis was used to identify the crystalline phases, crystal

structure, and crystallinity of the synthesized materials. The average crystallite size was estimated from the major diffraction peaks using the Scherrer equation, where applicable. UV–Vis spectroscopy was used to investigate the optical absorption characteristics of the samples and, where appropriate, to estimate their optical band-gap energies.

3.0 Results and Discussion

3.1 UV–Visible Spectroscopic Analysis

The UV–Visible absorption spectra of the synthesized MgO nanoparticles (MgONPs), ZnO nanoparticles (ZnONPs), and MgO–ZnO nanocomposite (MgO–ZnO NC) are presented in Fig.1. The spectra were recorded over the ultraviolet-to-visible wavelength region to examine the optical response and electronic-transition characteristics of the synthesized materials. All three samples exhibited pronounced absorption in the ultraviolet region, confirming their semiconductor/metal-oxide optical characteristics. However, differences in the position and intensity of the absorption features were observed following the combination of MgO and ZnO.

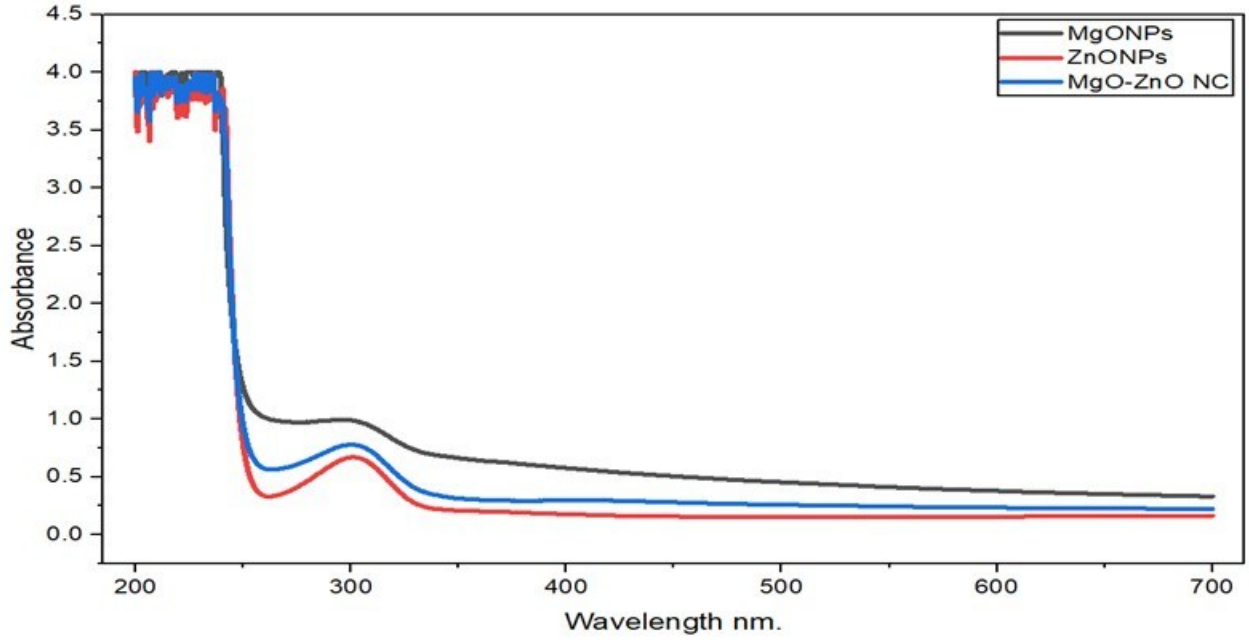

Fig. 1: UV–Visible absorption spectra of MgO nanoparticles, ZnO nanoparticles, and MgO–ZnO nanocomposite.

The MgONPs exhibited a principal absorption feature at approximately 305 nm, whereas the ZnONPs showed an absorption maximum near 302 nm. The MgO–ZnO NC exhibited a further shift of the principal absorption feature to approximately 298 nm (Eddy *et al*., 2026a)

$$E = \frac{hc}{\lambda_{max}} \qquad (1)$$

where h is the Planck constant, λ_{max} is the wavelength of absorption maxima, and cis thespeed of light. The corresponding photon energies calculated from equation 1 are approximately 4.07, 4.11, and 4.16 eV for MgONPs, ZnONPs, and MgO–ZnONC, respectively (Table 1). Thus, incorporation of MgO into ZnO was associated with an approximately 0.055 eV increase relative to ZnO and 0.096 eV relative to MgO in the energy corresponding to the observed absorption maximum.

The absorption of ZnONPs around 302 nm is consistent with the characteristic ultraviolet response associated with ZnO.

The MgONPs showed comparatively stronger absorbance in the UV region, with a broad absorption profile extending into the longer-wavelength region. This behavior may be associated with electronic transitions and surface-related states arising from the nanoscale MgO structure. In nanosized metal oxides, surface defects, oxygen vacancies, particle aggregation, and surface-bound species can contribute to broadening and modification of the absorption profile (Muhaymin et al., 2024). Therefore, the relatively broad spectral response observed for MgONPs may reflect contributions from both intrinsic electronic transitions and surface-related optical states.

Table 1. Absorption maxima and corresponding photon energies

Sample	Absorption maximum, λ_{max} (nm)	Photon energy, E (eV)
MgONPs	305	4.07
ZnONPs	302	4.11
MgO–ZnO NC	298	4.16

An important feature of Fig. 1 is the shift of the principal absorption maximum from 302 nm for ZnONPs to 298 nm for the MgO–ZnO NC. This approximately 4 nm hypsochromic (blue) shift corresponds to an increase in the photon energy from approximately 4.11 to 4.16 eV. Such a shift indicates that the optical response of ZnO was modified following the incorporation of MgO. The modification may originate from changes in the interfacial electronic environment, particle size, defect concentration, surface states, or interfacial interaction between MgO and ZnO. The effect is consistent with the possibility of electronic coupling at the MgO/ZnO interface, although UV–Visible spectroscopy alone cannot conclusively establish the mechanism of charge separation.

The MgO–ZnO NC also retained substantial absorption in the ultraviolet region while displaying a different absorption intensity profile from the individual oxide nanoparticles. This behavior is important for photocatalytic applications because the absorption of incident photons is the first step in photocatalytic charge generation. When the nanocomposite is irradiated with photons of sufficient energy, electron–hole pairs can be generated, after which interfacial interactions between MgO and ZnO may influence their migration and recombination. The existence of a closely connected MgO–ZnO interface observed in the HRSEM image (Fig. 2C) provides morphological evidence supporting the possibility of such interfacial interactions.

The UV–Visible results demonstrate that the synthesis of the MgO–ZnONC produced a measurable modification of the optical response of ZnO. The shift of the absorption maximum from 302 to 298 nm and the corresponding increase in photon energy from 4.11 to 4.16 eV indicate that MgO incorporation altered the optical environment of ZnO. These findings support the potential of the MgO–ZnO material for photocatalytic applications, although direct claims of enhanced charge separation or photocatalytic efficiency should be confirmed using photocatalytic kinetics, photoluminescence (PL), or electrochemical measurements.

3.2 High-Resolution Scanning Electron Microscopy (HRSEM)

[The HRSEM micrographs of the synthesized MgO nanoparticles (MgONPs), ZnO nanoparticles (ZnONPs), and MgO–ZnO nanocomposite (MgO–ZnO NC) are presented in Fig. 2. The micrographs reveal distinct differences in surface morphology, particle arrangement, aggregation behavior, surface roughness, and interfacial structure among the three samples.

The HRSEM image of the MgONPs in Fig. 2A, recorded at approximately 10,000×

magnification with a 1 μm scale bar, shows numerous closely packed particles with predominantly rounded to irregular morphologies. The particles are arranged in interconnected aggregates with a rough and heterogeneous surface texture. The observed aggregation is associated with the high surface energy of nanoscale MgO particles, which promotes interparticle attraction during nucleation, precipitation, drying, and subsequent thermal treatment. The micrograph also reveals appreciable interparticle spaces and surface irregularities, which contribute to the development of accessible surface regions for interactions with adsorbate molecules. The aggregated morphology indicates strong particle–particle interactions and the formation of interconnected MgO domains.

The ZnONPs shown in Fig. 2B exhibit a comparatively compact and heterogeneous morphology, with irregularly aggregated particles forming rough surface structures.

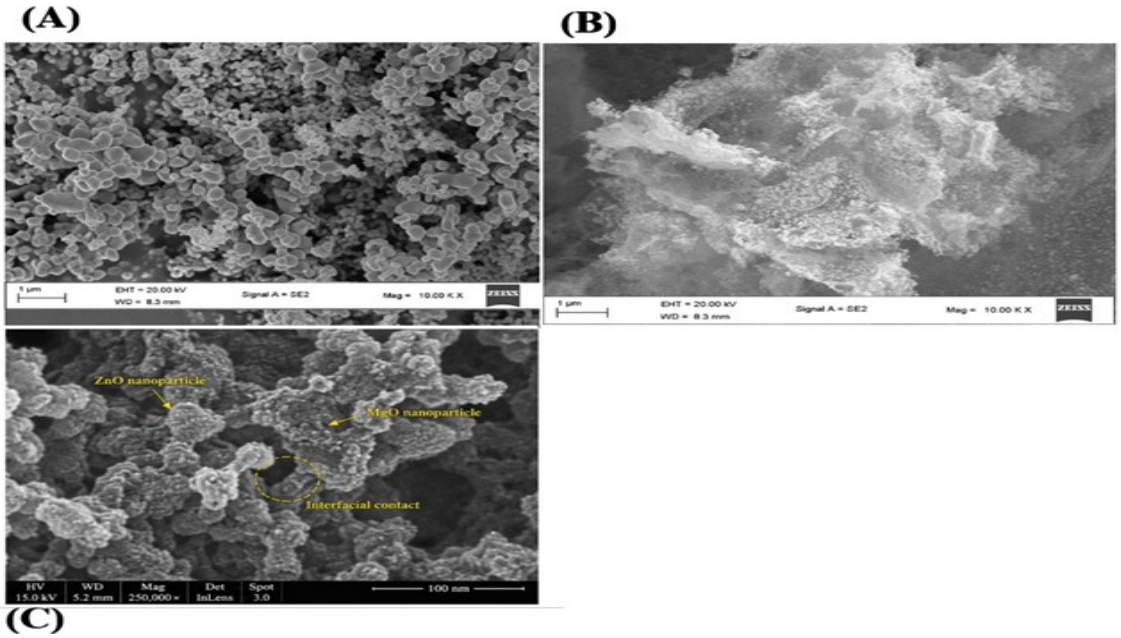

Fig. 2: **HRSEM images of (A) MgO nanoparticles, (B) ZnO nanoparticles, and (C) MgO–ZnO nanocomposite**

The relatively close packing of the particles may have resulted from nucleation and subsequent particle growth during synthesis and thermal processing. The rough and uneven surface provides numerous potential active sites for interaction with dye molecules and other organic pollutants during photocatalytic treatment. The morphology observed for the ZnONPs is consistent with the formation of nanoscale ZnO particles, although considerable interparticle aggregation is evident at the magnification employed. The relatively compact arrangement of ZnO particles also provides a suitable structural framework for subsequent incorporation of MgO.

A substantially different morphology is observed for the MgO–ZnO NC in Fig. 2C. The micrograph, recorded at approximately 250,000× magnification with a 100 nm scale bar, reveals a highly textured, interconnected, and heterogeneous nanoscale architecture. Distinct regions associated with ZnO and MgO are visible, with a clearly identifiable interfacial contact region between the two oxide phases. The close association of the MgO and ZnO domains indicates the formation of an integrated composite structure rather than

physically isolated oxide particles. The intimate contact between the two phases provides an effective interface for interfacial interaction and facilitates the modification of the physicochemical properties of ZnO following MgO incorporation.

The MgO–ZnO NC also exhibits a rough and porous-looking surface with numerous interparticle spaces. The interconnected architecture increases the accessibility of surface regions and provides potential adsorption sites for organic dye molecules. Such surface characteristics are particularly advantageous for photocatalytic applications because adsorption of pollutant molecules at or near the catalyst surface facilitates their interaction with photogenerated charge carriers and reactive oxygen species. The rough surface architecture may therefore contribute to improved surface reactivity and pollutant–catalyst interactions.

The reduced degree of large-scale aggregation observed in portions of the MgO–ZnO NC relative to the individual oxide nanoparticles can be attributed to the combined influence of the MgO and ZnO phases and the biogenic constituents present during synthesis. Phytochemicals in the *Moringa oleifera* leaf extract can interact with precursor ions and developing particle surfaces, thereby influencing nucleation, particle growth, and surface stabilization. The presence of MgO and ZnO domains also provides heterogeneous nucleation sites that can modify particle growth and produce the interconnected morphology observed in Fig. 2C. Consequently, the biogenic synthesis route contributes to the development of a structurally integrated MgO–ZnO nanocomposite with a rough and accessible surface.

The morphological differences among the three samples provide important information concerning their potential photocatalytic characteristics. The MgONPs exhibit pronounced aggregation and rough surface features, while the ZnONPs display comparatively compact and heterogeneous aggregates. In contrast, the MgO–ZnO NC possesses an interconnected architecture characterized by surface roughness, interparticle voids, and intimate contact between MgO and ZnO domains. These characteristics provide complementary structural advantages, including accessible surface sites for pollutant adsorption and closely associated oxide interfaces capable of facilitating interfacial charge-carrier transport.

The interfacial contact observed in Fig. 2C is particularly significant for the MgO–ZnO NC because the photocatalytic properties of semiconductor composites are strongly influenced by the nature and extent of contact between their constituent phases. The intimate association of MgO and ZnO provides an interfacial region through which photogenerated charge carriers can migrate, thereby promoting their spatial separation and reducing the probability of direct electron–hole recombination. This structural arrangement can enhance the availability of charge carriers for surface redox reactions involved in photocatalytic degradation.

Overall, the HRSEM results demonstrate distinct morphological characteristics for the three synthesized materials. The MgONPs exhibit aggregated and rough particles, the ZnONPs show compact and heterogeneous aggregates, whereas the MgO–ZnO NC displays a highly interconnected, rough, and porous surface with clearly observable MgO/ZnO interfacial contact. The formation of this integrated architecture demonstrates the successful development of the MgO–ZnO composite and provides a structural basis for its anticipated photocatalytic activity. The HRSEM observations are further supported by the UV–Visible spectral results, which show a modification of the optical absorption characteristics following the incorporation of MgO into ZnO.

3.3 Integrated Interpretation of HRSEM and UV–Visible Results

Table 2 summarizes the principal optical and morphological characteristics obtained from the UV–Visible and HRSEM analyses of the synthesized MgO, ZnO, and MgO–ZnO NC materials.

The UV–Visible data in Table 2 demonstrate a progressive shift in the absorption maximum from 305 nm for MgONPs to 302 nm for ZnONPs and 298 nm for the MgO–ZnONC. The corresponding photon energies calculated using E=1240/λE=1240/\lambda are 4.07, 4.11, and 4.16 eV, respectively. Thus, the MgO–ZnO NC exhibits a 4 nm shift toward shorter wavelength relative to ZnONPs, corresponding to an increase of approximately 0.055 eV in the photon energy associated with the absorption maximum. This change indicates that incorporation of MgO modifies the optical response of ZnO and alters the electronic environment of the resulting composite.

Table 2. Summary of optical and morphological properties of the synthesized nanoparticles

Parameter	MgO	ZnO	MgO–ZnONC
Absorption maximum	305 nm	302 nm	298 nm
Photon energy at λmax	4.07 eV	4.11 eV	4.16 eV
Shift relative to ZnO	—	—	4 nm toward shorter wavelength
Energy change relative to ZnO	—	—	+0.055 eV
SEM magnification	~10,000×	~10,000×	~250,000×
Scale bar	1 μm	1 μm	100 nm
Morphology	Aggregated/rough	Compact/aggregated	Interconnected/rough/porous
Clear MgO–ZnO interface	No	No	Visually indicated

The shift in the absorption maximum can be related to changes in the interfacial electronic structure, particle dimensions, defect states, and surface characteristics resulting from the combination of MgO and ZnO. The MgO–ZnO NC exhibits the highest photon energy at its principal absorption maximum, indicating a modified electronic transition relative to the individual oxide nanoparticles. The observed optical modification is consistent with interaction between the two oxide phases and the development of an MgO/ZnO interface.

The HRSEM results provide complementary structural evidence for the optical modification observed in the UV–Visible spectra. The individual MgONPs and ZnONPs exhibit aggregated morphologies, whereas the MgO–ZnO NC displays an interconnected nanoscale structure with clearly visible MgO/ZnO interfacial contact. The substantially higher magnification used for the MgO–ZnO NC reveals closely associated nanoscale domains and interparticle voids, demonstrating intimate contact between the two components. This interfacial architecture provides a pathway for interaction between the electronic structures of MgO and ZnO and contributes to the modified optical behavior observed for the composite.

The rough and interconnected surface of the MgO–ZnO NC is also relevant to its anticipated photocatalytic performance. The presence of interparticle spaces and heterogeneous surface features provides numerous accessible sites for adsorption of

organic dye molecules. The close contact between MgO and ZnO further provides interfacial regions through which photogenerated electrons and holes can participate in charge-transfer processes. Consequently, the combination of the modified optical response and interconnected surface architecture provides favorable physicochemical characteristics for photocatalytic applications.

The comparison presented in Table 2 therefore demonstrates that MgO incorporation produces simultaneous changes in the optical absorption characteristics and surface morphology of ZnO. The absorption maximum shifts from 302 to 298 nm, while the corresponding photon energy increases from 4.11 to 4.16 eV. At the same time, the morphology changes from the relatively compact and aggregated structure of ZnO to the rough, interconnected, and porous architecture of the MgO–ZnO NC. These combined changes indicate successful modification of ZnO through MgO incorporation and provide structural and optical evidence supporting the suitability of the synthesized MgO–ZnO NC for photocatalytic applications. The observed relationship between morphology and optical response is particularly important for dye degradation. The interconnected MgO–ZnO architecture provides accessible surface regions for adsorption, while the MgO/ZnO interface provides an electronically coupled region that facilitates the interaction of photogenerated charge carriers with the catalyst surface. Under irradiation, these characteristics can promote the generation and utilization of reactive oxygen species responsible for the oxidative degradation of organic dye molecules. Thus, the combined HRSEM and UV–Visible results establish that the biogenic synthesis route produced an MgO–ZnO nanocomposite with modified optical characteristics and a structurally integrated surface architecture suitable for application as a photocatalyst.

3.3 Energy-Dispersive X-ray Spectroscopy (EDS)

Energy-dispersive X-ray spectroscopy (EDS) was employed to determine the elemental composition of the synthesized MgO nanoparticles (MgONPs), ZnO nanoparticles (ZnONPs), and MgO–ZnO nanocomposite (MgO–ZnO NC). The corresponding EDS spectra are presented in Fig. 3. The technique provides elemental identification through the characteristic X-ray emission energies generated when the samples are irradiated with the electron beam during scanning electron microscopy.

3.3.1 EDS spectrum of MgO nanoparticles

The EDS spectrum of the MgONPs in Fig. 3A is dominated by characteristic signals corresponding to magnesium (Mg) and oxygen (O). The intense Mg signal in the low-energy region, together with the accompanying oxygen signal, provides direct elemental evidence for the formation of a magnesium–oxygen-based material. The strong Mg peak indicates that Mg is the predominant detectable metallic element in the synthesized material, while the oxygen signal confirms the presence of oxygen associated with the oxide phase.

A relatively weak carbon (C) signal is also visible in the spectrum. This minor carbon contribution is commonly associated with carbonaceous sample mounts, conductive carbon tape, residual organic species from the plant-mediated synthesis, or surface-adsorbed atmospheric carbon. The weak carbon signal does not constitute a dominant component of the sample and does not alter the principal Mg–O elemental composition observed in the spectrum. A minor Na signal is also apparent, which may originate from residual sodium-containing species associated with the NaOH used during precipitation. The weak chlorine-related feature may similarly be associated with

trace residual precursor-derived species or background contributions.

The dominance of Mg and O signals demonstrates that the principal elemental constituents of the synthesized material are consistent with MgO. The absence of prominent signals from other metallic elements indicates that no substantial extraneous metallic phase was detected by EDS within the analyzed region. Thus, the EDS result supports the formation of MgO nanoparticles and complements the morphological information obtained from HRSEM.

3.3.2 EDS spectrum of ZnO nanoparticles

The EDS spectrum of the ZnONPs in Fig. 3B exhibits prominent characteristic peaks corresponding to zinc (Zn) and oxygen (O). The Zn peaks are particularly intense and occur at the characteristic energies associated with Zn X-ray emission, including the prominent Zn L-series region at approximately 1 keV and higher-energy Zn K-series features around 8–9 keV. The oxygen signal occurs in the low-energy region and confirms the presence of oxygen associated with the ZnO phase.

The strong Zn signal relative to the other detected elements demonstrates that zinc is the major metallic constituent of the synthesized nanoparticles. The simultaneous detection of Zn and O is consistent with the formation of a zinc oxide-based material. The presence of minor carbon and low-intensity low-energy features can be associated with sample mounting, surface-adsorbed organic species, or residual constituents introduced during synthesis.

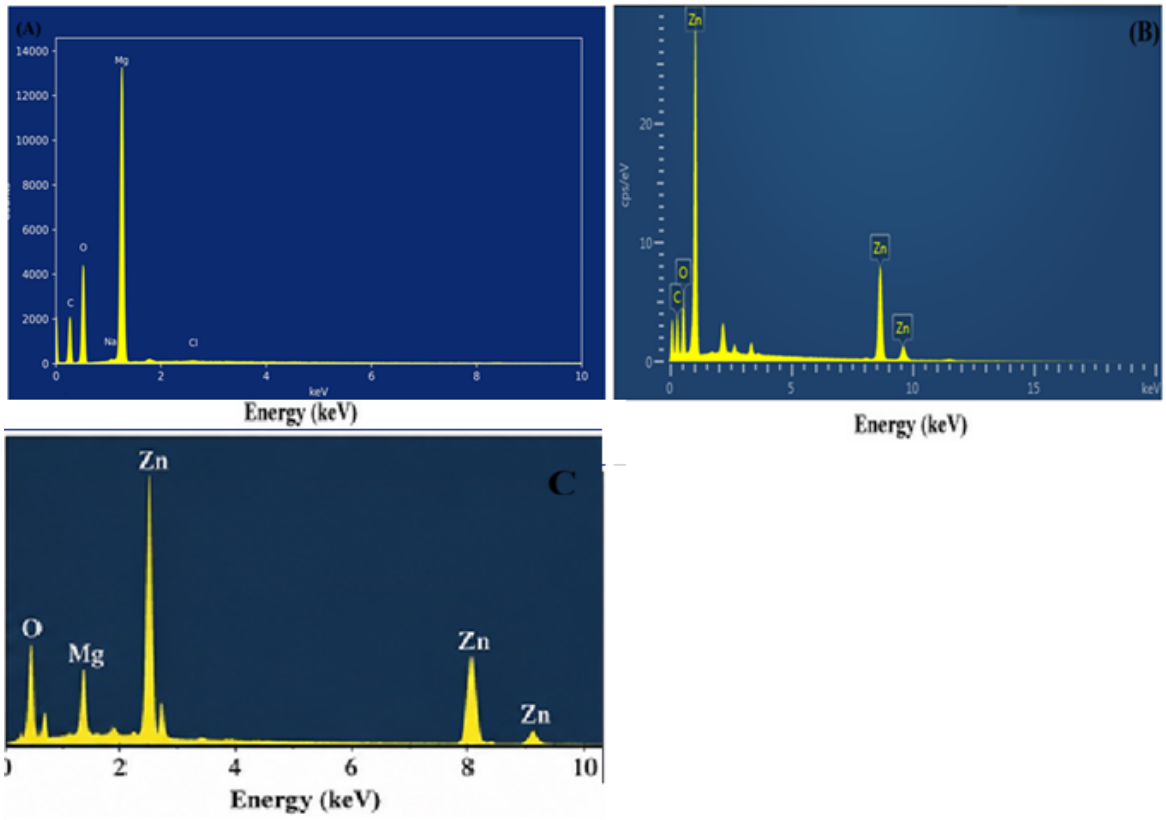

Fig. 3: EDS spectra of (A) MgO nanoparticles, (B) ZnO nanoparticles, and (C) MgO–ZnO nanocomposite

The EDS profile therefore provides elemental confirmation of the ZnO nanoparticles observed in the HRSEM analysis. In combination with the XRD data, the elemental composition can be correlated with the

crystalline phase and structural characteristics of the synthesized ZnO.

3.3.3 EDS spectrum of MgO–ZnO nanocomposite

A distinct change in the elemental profile is observed for the MgO–ZnO NC in Fig. 3C. The spectrum simultaneously exhibits characteristic peaks of Mg, Zn, and O, demonstrating the coexistence of magnesium, zinc, and oxygen within the analyzed region. The Zn signal is the most prominent metallic signal, reflecting the Zn-rich composition of the composite, while a clearly identifiable Mg peak confirms the incorporation of the Mg-containing component. The oxygen signal is also pronounced, consistent with the oxide nature of both MgO and ZnO.

The simultaneous detection of Mg and Zn in the same analyzed region is particularly significant. Whereas the EDS spectrum of MgONPs is dominated by Mg and O and that of ZnONPs by Zn and O, the MgO–ZnO NC contains all three principal elements. This elemental combination provides direct compositional evidence for the formation of a Mg–Zn–O material and supports the successful integration of the MgO and ZnO components during the biogenic synthesis process.

The spectrum in Fig. 3C also shows the characteristic Zn emission features at approximately the low-energy Zn L-series region and the higher-energy Zn K-series region. The Mg signal occurs in the low-energy region, while the oxygen peak is observed at approximately 0.5 keV. The simultaneous presence of these signals confirms the heterogeneous elemental composition expected for the MgO–ZnO composite.

The relative intensity of the Zn signal compared with the Mg signal is consistent with the synthesis formulation in which ZnO constitutes the principal oxide matrix while Mg-containing precursor was introduced at a lower molar proportion. Consequently, the EDS spectrum provides qualitative support for the successful incorporation of MgO into the ZnO-based material. The result is also consistent with the HRSEM observation of closely associated MgO and ZnO domains and the interfacial contact observed in Fig. 2C.

3.3.4 Comparative elemental interpretation

The EDS spectra demonstrate a systematic change in elemental composition from the individual oxides to the MgO–ZnO nanocomposite. MgONPs show the characteristic Mg and O signals, ZnONPs exhibit Zn and O signals, whereas the MgO–ZnO NC simultaneously displays Mg, Zn, and O signals. This progression is summarized in Table 3.

Table 3. Qualitative elemental composition of the synthesized materials based on EDS analysis

Sample	Principal elements detected	Dominant metallic element	Elemental interpretation
MgONPs	Mg, O	Mg	Consistent with MgO
ZnONPs	Zn, O	Zn	Consistent with ZnO
MgO–ZnO NC	Mg, Zn, O	Zn, with Mg present	Consistent with MgO–ZnO composite
MgO–ZnO NC	Minor C also observed	—	Carbon may originate from sample preparation and/or residual biogenic surface species

The EDS results provide strong complementary evidence for the successful formation of the MgO–ZnO nanocomposite. The detection of Mg, Zn, and O within the same

analyzed composite confirms that both oxide components are represented in the synthesized material. In particular, the appearance of the Mg signal together with the characteristic Zn and O signals demonstrates that Mg-containing material was incorporated into the ZnO-based structure rather than producing ZnO alone.

The elemental results are also consistent with the observed HRSEM morphology. Fig. 2C shows closely associated domains attributed to MgO and ZnO, while Fig. 3C demonstrates the simultaneous presence of Mg, Zn, and O in the corresponding material. The agreement between the morphological and elemental analyses therefore provides complementary evidence for the development of an integrated MgO–ZnO nanocomposite.

The presence of oxygen in all three samples is expected because oxygen constitutes the anionic component of both MgO and ZnO. The oxygen signal in the composite further indicates that the Mg- and Zn-containing species exist predominantly within an oxygen-containing matrix. The strong Zn response and comparatively lower Mg response in the composite are consistent with the ZnO-rich formulation used during synthesis, in which Mg was introduced as a modifying component. The weak carbon signals observed in the spectra are attributed to carbon-containing surface species, the sample mounting medium, or residual organic constituents associated with the *Moringa oleifera* extract used during the biogenic synthesis. The presence of such low-intensity carbon features is consistent with the use of a plant-mediated synthesis route and does not obscure the dominant Mg–Zn–O elemental composition of the nanocomposite.

3.3.5 Relationship between elemental composition and material properties

The EDS results have important implications for the structural and functional characteristics of the synthesized materials. The Mg and Zn elements provide the respective cationic components of MgO and ZnO, while oxygen forms the oxide framework. The coexistence of Mg and Zn in the MgO–ZnO NC establishes the chemical basis for interfacial interaction between the two oxide phases. Such interaction can modify the local electronic environment, surface characteristics, and charge-transfer behavior of the composite.

The elemental composition also complements the UV–Visible results, which showed a shift in the principal absorption maximum from 302 nm for ZnONPs to 298 nm for the MgO–ZnO NC. The simultaneous incorporation of Mg into the ZnO-containing material provides a compositional basis for the observed modification in optical response. Similarly, the Mg/Zn/O elemental distribution complements the HRSEM evidence of an interconnected and rough MgO–ZnO morphology.

The combined EDS and HRSEM results consequently establish both the elemental composition and morphological integration of the synthesized nanocomposite. The presence of Mg, Zn, and O, together with the observed intimate contact between MgO- and ZnO-associated domains, confirms the successful preparation of the MgO–ZnO material. The resulting combination of oxide composition, interconnected morphology, and interfacial contact provides favorable structural characteristics for surface adsorption and photocatalytic reactions involving organic pollutants.

Overall, the EDS analysis confirms that the synthesized MgONPs, ZnONPs, and MgO–ZnO NC possess the expected elemental constituents. The MgONPs are characterized predominantly by Mg and O, the ZnONPs by Zn and O, and the MgO–ZnO NC by Mg, Zn, and O. The appearance of Mg together with Zn and O in the composite provides direct elemental evidence of successful MgO modification of the ZnO-based material and, together with the HRSEM and UV–Visible results, supports the suitability of the

synthesized MgO–ZnO NC for photocatalytic wastewater-treatment applications.

3.4 X-ray Powder Diffraction (XRD) Analysis

The X-ray powder diffraction (XRD) patterns of the synthesized MgO nanoparticles (MgONPs), ZnO nanoparticles (ZnONPs), and MgO–ZnO nanocomposite (MgO–ZnO NC) are presented in Fig.4. The XRD analysis was used to determine the crystalline phases, crystal structures, phase composition, crystallinity, interplanar spacing, lattice parameters, and average crystallite sizes of the synthesized materials.

3.4.1 XRD Pattern of MgO Nanoparticles

The XRD pattern of the MgONPs in Fig. 4A exhibits well-defined diffraction peaks characteristic of crystalline magnesium oxide with a cubic face-centred cubic (FCC) structure. The major diffraction peaks occur at approximately 2θ = 36.9°, 42.9°, 62.3°, 74.7°, and 78.6°, corresponding to the (111), (200), (220), (311), and (222) crystallographic planes, respectively. These reflections are characteristic of cubic MgO and correspond to the standard JCPDS Reference Card No. 45-0946 for MgO.

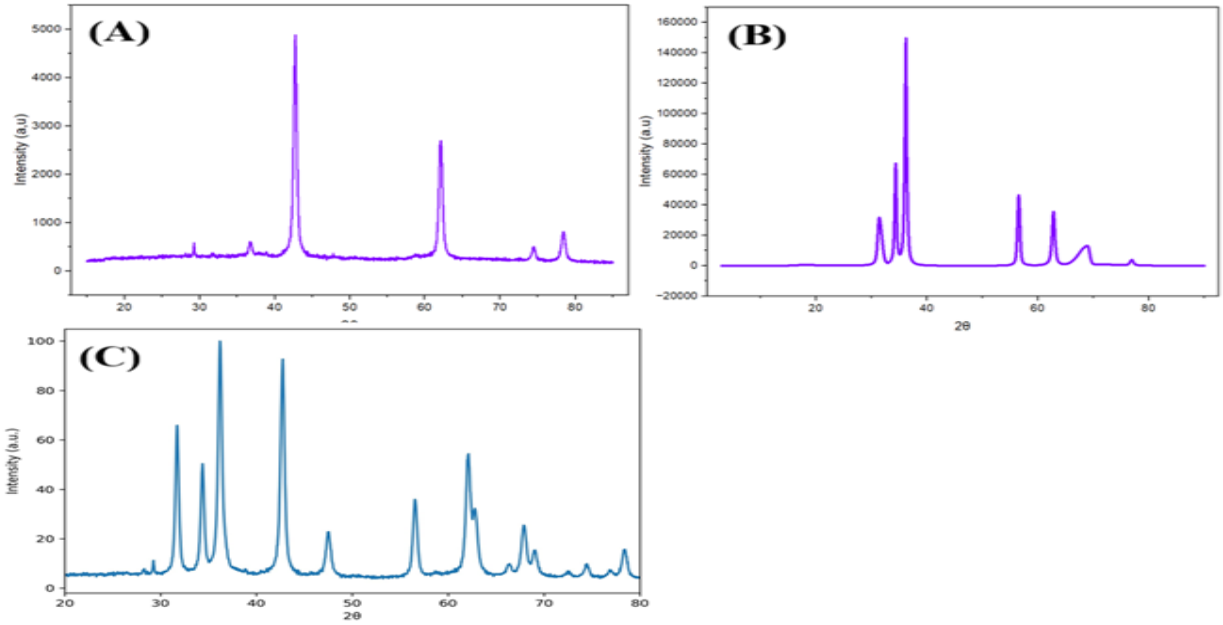

Fig. 4: XRD diffractograms of (A) MgO nanoparticles, (B) ZnO nanoparticles, and (C) MgO–ZnO nanocomposite

The intense peak at approximately 42.9° is assigned to the (200) plane and represents the dominant reflection of the synthesized MgO. The other prominent reflections at approximately 36.9°, 62.3°, 74.7°, and 78.6° correspond to the (111), (220), (311), and (222) planes, respectively. The agreement between the experimentally observed reflections and JCPDS No. 45-0946 confirms the formation of the cubic MgO phase.

The interplanar spacings were calculated using the Bragg's law, expressed as equation 2 (Eddy *et al*., 2023a,b)

$$n\lambda = 2\text{dain}\theta \qquad (1)$$

Where n = 1, λ =1.5406 Å for Cu Kα radiation, d is the interplanar spacing, and θ\theta is the Bragg angle. The calculated interplanar spacings are approximately 2.43 Å for (111), 2.11 Å for (200), 1.49 Å for (220), 1.27 Å for (311), and 1.22 Å for (222).

For the cubic MgO structure, the lattice parameter and unit volume were calculated using equations 3 and 4(Eddy *et al*., 2026a-c, 2024 a-b)

$$a = d\sqrt{h^2 + k^2 + l^2} \quad (3)$$

$$V = a^3 \quad (4)$$

The calculated lattice parameter is approximately 4.21 Å, while the corresponding unit-cell volume obtained from equation 4 is approximately 74.7 Å^3. These values are consistent with the cubic MgO structure represented by JCPDS Card No. 45-0946.The average crystallite size of the MgONPs was calculated using the Debye–Scherrer equation (equation 5) (Eddy *et al*.,2023b; Odeomelam *et al*.,2023)

$$d_{cryst} = \frac{k\lambda}{\beta cos\theta} \quad (5)$$

where d_{cryst} is the crystallite size, k is the Scherrer constant, λ is the X-ray wavelength, β is the FWHM of the diffraction peak in radians, and θ\theta is the Bragg angle. The calculated average crystallite size was 24.5 nm, confirming the nanoscale crystalline nature of the synthesized MgO.

3.4.2 XRD Pattern of ZnO Nanoparticles

The XRD pattern of the ZnONPs in Fig. 4B displays several sharp and intense diffraction peaks characteristic of hexagonal wurtzite ZnO. The principal reflections are observed at approximately 2θ = 31.7°, 34.4°, 36.2°, 47.5°, 56.6°, 62.9°, 66.4°, 67.9°, and 69.1°, corresponding to the (100), (002), (101), (102), (110), (103), (200), (112), and (201) planes, respectively. The observed reflections agree closely with the standard diffraction pattern of hexagonal wurtzite ZnO represented by JCPDS Reference Card No. 36-1451. The characteristic reflections at approximately 31.7°, 34.4°, and 36.2°, assigned to the (100), (002), and (101) planes, respectively, constitute the principal diffraction fingerprints of wurtzite ZnO. The presence of the additional reflections at higher 2θ values further confirms the development of a well-crystallized ZnO phase. The interplanar spacings calculated from Bragg's law (equation 2 are approximately 2.81 Å for (100), 2.60 Å for (002), 2.48 Å for (101), 1.91 Å for (102), and 1.63 Å for (110). For the hexagonal ZnO structure, the lattice parameters were determined using equation 6

$$\frac{1}{d^2} = \frac{(h^2+hk+k^2)}{a^2} \times \frac{l^2}{c^2} \quad (6)$$

The calculated lattice parameters are approximately a = b = 3.25 Å and c = 5.21 Å, with a corresponding c/a ratio of approximately 1.60. The unit-cell volume calculated from equation 7 is approximately 47.7 Å^3.

$$V = \frac{\sqrt{3}}{2} \times \frac{a^2 c}{1} \quad (7)$$

These structural parameters are consistent with the hexagonal wurtzite ZnO phase represented by JCPDS Card No. 36-1451. The average crystallite size calculated using the Debye–Scherrer equation was 28.6 nm, confirming that the synthesized ZnO consists of nanoscale crystalline domains. The sharpness and intensity of the diffraction peaks indicate a high degree of crystallinity.

3.4.3 XRD Pattern of MgO–ZnO Nanocomposite

The XRD pattern of the MgO–ZnO NC shown in Fig. 4C contains diffraction reflections corresponding to both cubic MgO and hexagonal wurtzite ZnO. The ZnO-associated reflections occur at approximately 31.7°, 34.4°, 36.2°, 47.5°, 56.6°, and 62.9°, corresponding to the (100), (002), (101), (102), (110), and (103) planes, respectively. These reflections correspond to JCPDS Card No. 36-1451.

The MgO-associated reflections occur at approximately 36.9°, 42.9°, 62.3°, 74.7°, and 78.6°, corresponding to the (111), (200), (220), (311), and (222) planes, respectively, and are indexed according to JCPDS Card No. 45-0946. The simultaneous presence of reflections indexed to JCPDS No. 45-0946 (MgO) and JCPDS No. 36-1451 (ZnO) provides direct crystallographic evidence for the coexistence of the two crystalline oxide phases in the MgO–

ZnO NC. The retention of the characteristic MgO and ZnO reflections after composite formation indicates that MgO modification did not destroy the fundamental crystal structures of either component.

The XRD pattern of the composite also exhibits changes in relative peak intensity and peak profile compared with the individual oxides. These changes are associated with the coexistence of the two crystalline phases, their relative proportions, crystallographic orientations, and interfacial interactions. The composite therefore retains the characteristic crystalline structures of MgO and ZnO while exhibiting a modified diffraction profile arising from their intimate association.

The average crystallite size of the MgO–ZnO NC was calculated as 26.1 nm using the Debye–Scherrer equation. This value is intermediate between the crystallite sizes of MgO (24.5 nm) and ZnO (28.6 nm). Relative to ZnO, the incorporation of MgO resulted in an approximately 8.74% reduction in average crystallite size equal to 8.74\%. The crystallite size of the MgO–ZnO NC was approximately 6.53% higher than that of MgO equal to 6.53\% The intermediate crystallite size of the composite indicates that MgO incorporation influenced the crystal-growth process of ZnO. The presence of Mg-containing species can provide additional nucleation sites and interfacial boundaries that restrict excessive growth of ZnO crystallites. In addition, phytochemical constituents from the *Moringa oleifera* leaf extract can participate in nucleation and surface stabilization, contributing to the formation of nanoscale crystallites.

3.4.4 Phase Identification Based on JCPDS Reference Cards

The phase identification of the synthesized materials was performed by comparing the observed diffraction peaks with standard JCPDS reference patterns. The MgONPs exhibit diffraction reflections corresponding to JCPDS Card No. 45-0946, which represents crystalline cubic MgO. The principal MgO reflections are indexed as (111), (200), (220), (311), and (222). Detailed information is shown in Table 5

The ZnONPs exhibit the characteristic diffraction pattern of hexagonal wurtzite ZnO corresponding to JCPDS Card No. 36-1451. The principal ZnO reflections are indexed as (100), (002), (101), (102), (110), (103), (200), (112), and (201).For the MgO–ZnO NC, the diffraction pattern contains the characteristic reflections of both JCPDS Card No. 45-0946 for MgO and JCPDS Card No. 36-1451 for ZnO. Thus, the composite can be described crystallographically as a two-phase MgO–ZnO material consisting of cubic MgO and hexagonal wurtzite ZnO.

The JCPDS-based phase analysis provides clear evidence that the synthesized MgO–ZnO NC contains the two intended crystalline phases. The diffraction reflections of the composite correspond to JCPDS Card No. 45-0946 for MgO and JCPDS Card No. 36-1451 for ZnO, with no prominent unidentified crystalline reflections. The preservation of the characteristic MgO and ZnO reflections confirms that both oxide phases remain crystalline after the biogenic synthesis and calcination process.

3.4.5 Correlation of XRD, HRSEM and EDS Results

The XRD findings are consistent with the HRSEM and EDS results. HRSEM revealed an interconnected morphology with intimate contact between MgO- and ZnO-associated domains, while EDS confirmed the simultaneous presence of Mg, Zn, and O in the composite. XRD further established that these elements are associated with crystalline MgO and ZnO phases corresponding to JCPDS Card Nos. 45-0946 and 36-1451, respectively.

The combined characterization results therefore establish the successful formation of the MgO–ZnO nanocomposite. The nanoscale

crystallite size of 26.1 nm, retention of both crystalline phases, and intimate MgO/ZnO interfacial structure provide favorable characteristics for photocatalytic applications. The coexistence of MgO and ZnO phases creates an interfacial region capable of influencing photogenerated charge-carrier migration, while the nanoscale dimensions and rough interconnected morphology provide accessible surface regions for pollutant adsorption and photocatalytic reactions.

Table 5. XRD phase identification and crystallographic parameters

Parameter	MgO nanoparticles	ZnO nanoparticles	MgO–ZnO nanocomposite
JCPDS reference card	No. 45-0946	No. 36-1451	No. 45-0946 + No. 36-1451
Crystal structure	Cubic FCC	Hexagonal wurtzite	Cubic MgO + hexagonal ZnO
Space group	Fm-3m	$P6_3mc$	Fm-3m + $P6_3mc$
Principal reflections	(111), (200), (220), (311), (222)	(100), (002), (101), (102), (110), (103), (200), (112), (201)	MgO + ZnO reflections
Average crystallite size	24.5 nm	28.6 nm	26.1 nm
Lattice parameter, aa	~4.21 Å	~3.25 Å	Both phases retained
Lattice parameter, cc	—	~5.21 Å	ZnO phase retained
c/ac/a ratio	—	~1.60	—
Unit-cell volume	~74.7 $Å^3$	~47.7 $Å^3$	Two-phase structure
Phase identified	MgO	ZnO	MgO + ZnO

The XRD analysis confirms that the synthesized material is a crystalline two-phase MgO–ZnO nanocomposite comprising cubic MgO and hexagonal wurtzite ZnO, indexed to JCPDS Card No. 45-0946 and JCPDS Card No. 36-1451, respectively. The average crystallite sizes of MgO, ZnO, and MgO–ZnO NC were 24.5, 28.6, and 26.1 nm, respectively. The XRD, HRSEM, and EDS results collectively establish the successful formation of the intended MgO–ZnO nanocomposite and its suitability for subsequent evaluation as a photocatalyst for organic-pollutant degradation.

4.0 Conclusion

This study successfully demonstrated the biogenic synthesis of an MgO–ZnO nanocomposite using Moringa oleifera leaf extract as an environmentally friendly synthesis medium. The UV–Visible analysis showed characteristic ultraviolet absorption maxima at 305, 302, and 298 nm for MgO nanoparticles, ZnO nanoparticles, and the MgO–ZnO nanocomposite, respectively. The corresponding photon energies were 4.07, 4.11, and 4.16 eV, indicating a measurable modification of the optical response following MgO incorporation into ZnO.

HRSEM analysis revealed distinct morphological characteristics for the synthesized materials. MgO exhibited aggregated and rough particles, while ZnO showed relatively compact aggregated structures. In contrast, the MgO–ZnO nanocomposite exhibited a rough, interconnected and porous morphology with intimate contact between MgO- and ZnO-associated domains. This structural configuration provides accessible surface regions that can facilitate adsorption and surface reactions during photocatalytic treatment.

EDS analysis confirmed the presence of Mg and O in MgO, Zn and O in ZnO, and Mg, Zn, and O in the MgO–ZnO nanocomposite. XRD analysis further confirmed the crystalline nature of the synthesized materials, with MgO exhibiting a cubic FCC structure corresponding to JCPDS Card No. 45-0946, while ZnO exhibited a hexagonal wurtzite structure corresponding to JCPDS Card No. 36-1451. The MgO–ZnO nanocomposite retained the characteristic diffraction reflections of both phases, confirming the formation of a crystalline two-phase MgO–ZnO heterostructure. The average crystallite sizes of MgO, ZnO, and MgO–ZnO were 24.5, 28.6, and 26.1 nm, respectively, confirming their nanoscale crystalline dimensions.

The combined UV–Visible, HRSEM, EDS, and XRD results demonstrate that incorporation of MgO substantially modified the optical, morphological, elemental, and crystallographic characteristics of ZnO. The nanoscale crystallite size, interconnected surface morphology, and intimate MgO/ZnO interfacial contact provide favorable physicochemical characteristics for photocatalytic applications. The study therefore establishes Moringa oleifera-mediated synthesis as a viable green route for producing MgO–ZnO nanocomposites and provides a sustainable materials platform with potential application in the photocatalytic treatment of dye-contaminated wastewater.

Acknowledgement

The financial assistance of TETfund IBR (TETfund/DR&R/CE/UNI/Osara/IBR/2025/VOL 1/30) of CUSTECH Osara, Kogi, Nigeria, is acknowledged

5,0 References

Abdulkadir, A., Musah, M., Lakan, I. I., & Mathew, J. T. (2025). Production of MgO/ZnO nanocomposite for the removal of selected toxic metals from tannery wastewater. *Scholars International Journal of Chemistry and Material Sciences*, 8, 5, pp. 250–262. https://doi.org/10.36348/sijcms.2025.v08i05.008

Ahmed, R., Li, Y., & Hassan, M. (2023). Recent advances in green nanotechnology for environmental remediation: Focus on dye degradation. *Environmental Nanotechnology, Monitoring & Management*, 20, 100749. https://doi.org/10.1016/j.enmm.2023.100749

Alhamdany, S. R., Alsalhy, Q. F., Hassan, A. K., Al-Saadi, S., Meskher, H., & Al-Juboori, R. A. (2026). Eco-friendly synthesis of metal oxide nanoparticles (ZnO, MgO, and CuO) for efficient water purification: A review. *Materials Today Communications*, 51, 114845. https://doi.org/10.1016/j.mtcomm.2026.114845

Arafa, W. A., Nayl, A. A., Alanazi, A. H., Ahmed, I. M., Abdelwahab, A. A., Ibrahim, H. M., Bräse, S., & Nassar, A. M. (2026). Bifunctional recyclable ZnO/MgO nanocomposite: Solvent-free synthesis of chromenes and efficient water remediation. *Scientific Reports*, 16, 1. https://doi.org/10.1038/s41598-026-43572-y

Awad, H., Hamdy, K., Yasser, Y., Magdy, S., Phlip, N., Fawzy, N., Ashraf, F., & Mohammed, R. (2026). Plasmonic and

magnetic ZnO-based nanocomposites for enhanced photocatalysis and ultrasensitive SERS detection of malachite green. *Scientific Reports*, 16, 1. https://doi.org/10.1038/s41598-026-51090-0

Baba, I. A., Mustapha, S., Obayomi, O. V., Awe, O. B., Mustapha, L. S., & Obayomi, K. S. (2026). Advanced perspectives on nanoparticle engineering: Green innovations and characterization techniques. *Next Nanotechnology*, 9, 100499. https://doi.org/10.1016/j.nxnano.2026.100499

Bamisaye, A., Adekola, M. A., Abati, S. M., Etafo, N. O., Ademola, O. S., Joseph, P. T., Samuel, O., Ogunlaja, O. O., Langmi, H., & Idowu, M. A. (2025). Recent advances in metal/metal-oxide nanoparticle-polymer nanohybrid for biomedical applications. *Materials Today Chemistry*, 49, 103086. https://doi.org/10.1016/j.mtchem.2025.103086

Bognár, S., Putnik, P., & Šojić Merkulov, D. (2022). Sustainable green nanotechnologies for innovative purifications of water: Synthesis of the nanoparticles from renewable sources. *Nanomaterials*, 12, 2, 263. https://doi.org/10.3390/nano12020263

Deng, Y., Wang, X., & Yu, L. (2020). ZnO-based nanomaterials for photocatalytic degradation of organic pollutants: A review. *Journal of Environmental Chemical Engineering*, 8, 4, 103962. https://doi.org/10.1016/j.jece.2020.103962

Du, Y., Wu, S., Feng, T., & Jiang, W. (2026). MgO-loaded magnetic crab shell-derived biochar for efficient synergistic adsorption of heavy metals and dye: Characterization, adsorption performance and mechanistic study. *Nanomaterials*, 16, 3, 214. https://doi.org/10.3390/nano16030214

Ebrahimi, S., Zanganeh, P., Nouripour-Sisakht, S., Javadian, H., Babaie, A., Khaleghi, R., & Asfaram, A. (2026). A multifunctional graphene oxide-ZnO nanohybrid for rapid and highly efficient malachite green adsorption and strong broad-spectrum antimicrobial activity. *Scientific Reports*, 16, 1, 7316. https://doi.org/10.1038/s41598-026-36097-x

Eddy, N. O., Edet, U. E., Oladele, J. O., Kelle, H. I., Ogoko, E. C., Odiongenyi, A. O., Ameh, P., Ukpe, R. A., Ogbodo, R., Garg, R., & Garg, R. (2023b). Synthesis and application of novel microporous framework of nanocomposite from trona for photocatalysed degradation of methyl orange dye. *Environmental Monitoring and Assessment*. https://doi.org/10.1007/s10661-023-12014-x

Eddy, N. O., Eze, I. S., Adukwu, I. D., Garg, R., Garg, R., Taziwa, R., & Watandost, H. (2026a). Synthesis and characterization of limestone derived biphasic calcium silicate nanocomposites for coating and fuel cell applications. *Discover Materials*. https://doi.org/10.1007/s43939-026-00819-9

Eddy, N. O., Garg, R., Ukpe, R. A., Ameh, P. O., Gar, R., Musa, R., , Kwanchi, D., Wabaidur, S. M., Afta, S., Ogbodo, R., Aikoye, A. O., and Siddiqu, M. (2024). Application of periwinkle shell for the synthesis of calcium oxide nanoparticles and in the remediation of Pb^{2+}-contaminated water. *Biomass Conversion and Biorefinery,* 15, pp. 23939–23957. DOI: 10.1007/s13399-024-05285-y.

Eddy, N. O., Jibrin, J. I., Ukpe, R. A., Odiongenyi, A., Iqbal, A., Kasiemobi, A. M., Oladele, J. O., & Runde, M. (2024). Experimental and Theoretical Investigations of Photolytic and Photocatalysed Degradations of Crystal Violet Dye (CVD) in Water by oyster shells derived CaO nanoparticles (CaO-NP), *Journal of*

Hazardous Materials Advances, 13, 100413, https://doi.org/10.1016/j.hazadv.2024.100413

Eddy, N. O., Nweze, S., Eze, I. S., Garg, R., Taziwa, R., & Watandost, H. (2026b). Synthesis, characterisation and electrochemical behaviour of calcium carbonate nanoparticles derived from automobile oxy-acetylene gas welding waste. *Discover Nano, 21*, Article 360. https://doi.org/10.1186/s11671-026-04796-z

Eddy, N. O., Oladede, J., Eze, I. S., Garg, R., Garg, R., & Paktin, H. (2024b). Synthesis and characterization of CaO nanoparticles from periwinkle shells for the treatment of tetracycline-contaminated water by adsorption and photocatalyzed degradation. *Results in Engineering*, *103374*. https://doi.org/10.1016/j.rineng.2024.103374

Eddy, N. O., Udeokpote, G. C., Ekele, D. O., Garg, R., Garg, R., & Paktin, H. (2026c). Synthesis of carbon quantum dots using unutilized low-grade lignite coal. *BMC Chemistry*. https://doi.org/10.1186/s13065-026-01798-x

Eddy, N. O., Ukpe, R. A., Ameh, P., Ogbodo, R., Garg, R., & Garg, R. (2023a). Theoretical and experimental studies on photocatalytic removal of methylene blue (MetB) from aqueous solution using oyster shell synthesized CaO nanoparticles (CaONP-O). *Environmental Science and Pollution Research*. https://doi.org/10.1007/s11356-022-22747-w

Ganta, D. D., Bekele, S. G., Edossa, G. D., Zeleke, T. D., & Zereffa, E. A. (2026). Phyto-mediated synthesis of M-ZT/bentonite nanocomposite using *Hagenia abyssinica* for synergistic photocatalytic and antimicrobial efficacy. *Scientific Reports*, 16, 1. https://doi.org/10.1038/s41598-026-45345-z

Govindhan, M. (2025). Structural and optical engineering of MgO-ZnO nanocomposite via photon-induced method. *Ceramics International*, 51, 18, pp.26107–26114. https://doi.org/10.1016/j.ceramint.2025.03.295

Guerram, A., Khaled, B., Laouini, S. E., Bouafia, A., Amor, I. B., Barani, D., Zaghbib, I., Abdullah, M. M. S., Al-Lohedan, H. A., & Abdullah, J. A. A. (2026). MgO and MgO/char nanocomposites as efficient catalysts for the removal of thiophene and malachite green from aqueous systems. *Journal of Sol-Gel Science and Technology*, 118, 1. https://doi.org/10.1007/s10971-026-07145-9

Guo, T., Ikuta, T., & Li, C. (2026). Fabrication of high-crystallinity ZnO nanorods for photocatalytic application. *Inorganics*, 14, 6, 145. https://doi.org/10.3390/inorganics14060145

Hao, S., Ching, S. W., Tiong, T. J., Yap, Y. H., & Huang, C.-M. (2026). Photocatalytic performance of the synergetic coupling of NiO-MgO nanostructures on a g-C_3N_4 composite towards methylene blue under visible-light irradiation. *Journal of Composites Science*, 10, 1, 45. https://doi.org/10.3390/jcs10010045

Huang, Z., Zhu, J., Hu, Y., Zhu, Y., Zhu, G., Hu, L., Zi, Y., & Huang, W. (2022). Tin oxide (SnO_2) nanoparticles: Facile fabrication, characterization, and application in UV photodetectors. *Nanomaterials*, 12, 4, 632. https://doi.org/10.3390/nano12040632

Iriqui-Razcón, J. L., De-la-Cruz-Estrella, J. L., Brown-Bojórquez, F., Higuera-Valenzuela, H. J., Hernández-Abril, P. A., Maldonado-Arriola, J. A., & Heredia-Cancino, J. A. (2026). Green synthesis of ZnO nanoparticles using *Ocimum basilicum* var. *purpurascens*: As-synthesized phase formation and thermal

evolution of optical properties. *Nanomaterials*, 16, 10, 572. https://doi.org/10.3390/nano16100572

Jannat, M. R., Biswas, B., Rahman, M. L., Ahmed, M. F., Hossain, M. J., Khanam, J., & Sharmin, N. (2025). Validity of crystallite size determination methods based on XRD peak broadening in pure and metal-doped nickel ferrites. *Results in Materials*, 28, 100762. https://doi.org/10.1016/j.rinma.2025.100762

Kasi, G., Stalin, N., Rachtanapun, P., Jantanasakulwong, K., Halder, J. N., Phongthai, S., Worajittiphon, P., Seo, J., & Thanakkasaranee, S. (2025). Effect of calcination temperatures on crystallite size, particle size, and antimicrobial activity of synthesized MgO and its cytotoxicity. *International Journal of Molecular Sciences*, 26, 10, 4868. https://doi.org/10.3390/ijms26104868

Kumar, P., Sharma, S., & Pandey, A. (2022). Enhanced photocatalytic activity of MgO-doped ZnO nanocomposites synthesized via sol-gel method for dye degradation. *Materials Today: Proceedings*, 56, pp. 388–394. https://doi.org/10.1016/j.matpr.2022.03.326

Morgan, R. N., & Aboshanab, K. M. (2024). Green biologically synthesized metal nanoparticles: Biological applications, optimizations and prospects. *Future Science OA*, 10, 1, FSO935. https://doi.org/10.2144/fsoa-2023-0196

Muhaymin, A., Mohamed, H. E. A., Hkiri, K., Safdar, A., Azizi, S., & Maaza, M. (2024). Green synthesis of magnesium oxide nanoparticles using *Hyphaene thebaica* extract and their photocatalytic activities. *Scientific Reports*, 14, 1, 20135. https://doi.org/10.1038/s41598-024-71149-0

Nasiri, S., Rabiei, M., Palevicius, A., Janusas, G., Vilkauskas, A., Nutalapati, V., & Monshi, A. (2023). Modified Scherrer equation to calculate crystal size by XRD with high accuracy: Examples of Fe_2O_3, TiO_2 and V_2O_5. *Nano Trends*, 3, 100015. https://doi.org/10.1016/j.nwnano.2023.100015

Raha, S., & Ahmaruzzaman, M. (2022). ZnO nanostructured materials and their potential applications: Progress, challenges and perspectives. *Nanoscale Advances*, 4, 8, pp. 1868–1925. https://doi.org/10.1039/D1NA00880C

Reddy, N. R., Kumar, M. P., & Maheswari, U. (2022). Plant-mediated green synthesis of metal oxide nanoparticles and their application in wastewater treatment: A critical review. *Environmental Research*, 204, 111964. https://doi.org/10.1016/j.envres.2021.111964

Ruiz-Duarte, E. V., Molina-Jiménez, J. P., Ávila, D. A., Torres, C. O., & Horta-Piñeres, S. D. (2025). Rapid synthesis of highly crystalline ZnO nanostructures: Comparative evaluation of two alternative routes. *Crystals*, 15, 7, 640. https://doi.org/10.3390/cryst15070640

Sales, D. A., Jerônimo, A. G., Romaguera-Barcelay, Y., Del Mar Orta, M., Almeida, L. C., Viana, B. C., & Peña-Garcia, R. R. (2026). Relationship between lattice strain, defect redistribution, and photocatalytic response in Cr^{3+}/Al^{3+} co-doped ZnO micro–nanostructured systems. *Materials Chemistry and Physics*, 35132411. https://doi.org/10.1016/j.matchemphys.2026.132411

Sarmah, M., Deka, M., & Chutia, P. (2021). Photocatalytic degradation of hazardous dyes using metal oxide nanoparticles under visible light: A review. *Materials Today: Proceedings*, 43, pp. 392–399. https://doi.org/10.1016/j.matpr.2020.06.359

Selim, S., Almuhayawi, M. S., Saddiq, A. A., Alruhaili, M. H., Saied, E., Sharaf, M. H., Tarabulsi, M. K., & Al Jaouni, S. K. (2025). Synthesis of novel MgO-ZnO

nanocomposite using *Pluchea indica* leaf extract and study of their biological activities. *Bioresources and Bioprocessing*, 12, 1, 33. https://doi.org/10.1186/s40643-025-00848-x

Sivaranjani, S., Rajkumar, K., & Rajesh, V. (2022). Toxicological and ecological risk assessment of synthetic dyes in aquatic systems: An overview. *Ecotoxicology and Environmental Safety*, 233, 113318. https://doi.org/10.1016/j.ecoenv.2022.113318

Swamy, K. R., Shyamala, G., Gurugubelli, T. R., Ravindran, G., & Bathula, B. (2026). Recent advancements of wastewater treatment by photocatalysis: A comprehensive review. *iScience*, 29, 6, 116088. https://doi.org/10.1016/j.isci.2026.116088

Tanweer, T., Rana, N. F., Saleem, I., Shafique, I., Alshahrani, S. M., Almukhlifi, H. A., Alotaibi, A. S., Alshareef, S. A., & Menaa, F. (2022). Dental composites with magnesium-doped zinc oxide nanoparticles prevent secondary caries in the alloxan-induced diabetic model. *International Journal of Molecular Sciences*, 23, 24,15926. https://doi.org/10.3390/ijms232415926

Verma, A., Singh, R., & Ghosh, N. (2023). Biogenic synthesis of metal oxide nanostructures: An emerging green approach for photocatalytic and antimicrobial applications. *Green Chemistry Letters and Reviews*. https://doi.org/10.1080/17518253.2023.2165815

Wu, C., Liu, Z., & Zhang, J. (2025). Development and enhancement of charge separation processes for the degradation of RhB using an innovative ZnO/$MgIn_2S_4$ S-scheme heterojunction photocatalyst. *Journal of Physics and Chemistry of Solids*, 207, pp. 112901. https://doi.org/10.1016/j.jpcs.2025.112901

Zango, Z. U., Garba, A., Shittu, F. B., Imam, S. S., Haruna, A., Zango, M. U., Wadi, I. A., Bello, U., Adamu, H., Keshta, B. E., Bokov, D. O., Baigenzhenov, O., & Hosseini-Bandegharaei, A. (2025). A state-of-the-art review on green synthesis and modifications of ZnO nanoparticles for organic pollutants decomposition and CO_2 conversion. *Journal of Hazardous Materials Advances*, 17, 100588. https://doi.org/10.1016/j.hazadv.2024.100588

Zhu, C., & Wang, X. (2025). Nanomaterial ZnO synthesis and its photocatalytic applications: A review. *Nanomaterials*, 15, 9, 682. https://doi.org/10.3390/nano1509068

Compliance with Ethical Standards

Declaration

Ethical Approval

Not Applicable

Competing interests

The author declares no known competing financial interests.

Funding

This work was funded by TETfund through Institutional Based Research grant (TETfund/DR&R/CE/UNI/Osara/IBR/2025/VOL 1/30) of CUSTECH Osara, Kogi, Nigeria,.

Author's Contribution

The author conceived the study, conducted the legal and comparative analysis, verified the sources, and prepared the manuscript.